SCIENCE CHINA
Physics, Mechanics & Astronomy

Explanations of the DAMPE high energy electron/positron spectrum in the dark matter annihilation and pulsar scenarios

Wang BingBing, Bi XiaoJun, Lin SuJie and Yin PengFei

Citation: SCIENCE CHINA Physics, Mechanics & Astronomy **61**, 101004 (2018); doi: 10.1007/s11433-018-9244-y

View online: http://engine.scichina.com/doi/10.1007/s11433-018-9244-y

View Table of Contents:http://engine.scichina.com/publisher/scp/journal/SCPMA/61/10

Published by the Science China Press

SCIENCE CHINA
Physics, Mechanics & Astronomy

SCIENCE CHINA
Physics, Mechanics & Astronomy

• Article •
Special Topic: The Impact of DAMPE Results on Dark Matter Indirect Searches

October 2018 Vol. 61 No. 10: 101004
https://doi.org/10.1007/s11433-018-9244-y

Explanations of the DAMPE high energy electron/positron spectrum in the dark matter annihilation and pulsar scenarios

BingBing Wang[1,2], XiaoJun Bi[1], SuJie Lin[1], and PengFei Yin[1*]

[1] *Key Laboratory of Particle Astrophysics, Institute of High Energy Physics, Chinese Academy of Sciences, Beijing 100049, China;*
[2] *University of Chinese Academy of Sciences, Beijing 100049, China*

Received April 13, 2018; accepted May 11, 2018; published online August 9, 2018

Many studies have shown that either the nearby astrophysical source or dark matter (DM) annihilation/decay can be used to explain the excess of high energy cosmic ray (CR) $e^{\pm}$, which is detected by many experiments, such as PAMELA and AMS-02. Recently, the dark matter particle explorer (DAMPE) collaboration has reported its first result of the total CR $e^{\pm}$ spectrum from 25 GeV to 4.6 TeV with high precision. In this work, we study the DM annihilation and pulsar interpretations of this result. We show that the leptonic DM annihilation channels to $\tau^+\tau^-$, 4μ, 4τ, and mixed charged lepton final states can well explain the DAMPE $e^{\pm}$ spectrum. We also find that the mixed charged leptons channel would lead to a sharp drop structure at $\sim$ TeV. However, the ordinary DM explanations have been almost excluded by the constraints from the observations of gamma-ray and CMB, unless some exotic DM models are introduced. In the pulsar scenario, we analyze 21 nearby known pulsars and assume that one of them dominantly contributes to the high energy CR $e^{\pm}$ spectrum. Involving the constraint from the Fermi-LAT observation of the $e^{\pm}$ anisotropy, we find that two pulsars could explain the DAMPE $e^{\pm}$ spectrum. Our results show that it is difficult to discriminate between the DM annihilation and single pulsar explanations of high energy $e^{\pm}$ with the current DAMPE result.

cosmic rays, dark matter, pulsars

PACS number(s): 98.70.Sa, 95.35.+d, 97.60.Gb

Citation: B. B. Wang, X. J. Bi, S. J. Lin, and P. F. Yin, Explanations of the DAMPE high energy electron/positron spectrum in the dark matter annihilation and pulsar scenarios, Sci. China-Phys. Mech. Astron. **61**, 101004 (2018), https://doi.org/10.1007/s11433-018-9244-y

1 Introduction

After the cosmic ray (CR) $e^{\pm}$ excess above 10 GeV was confirmed by PAMELA and AMS-02 with high precision [1, 2], many models for its origin have been proposed in the literature. Two kinds of sources, including dark matter (DM) annihilation/decay in the Galactic halo [3-9] and nearby astrophysical sources [10-15], are widely used to explain the experimental data. Although the measurements of AMS-02 are unprecedentedly precise, the current results are not sufficient to distinguish between these two explanations [16].

Recently, the dark matter particle explorer (DAMPE) collaboration has reported its first result of the total CR $e^{\pm}$ spectrum in the energy range from 25 to 4.6 TeV [17]. The DAMPE satellite launched on Dec. 17, 2015 is a multipurpose detector, which consists of a Plastic scintillator strip detector (PSD), a silicon-tungsten tracker-converter (STK), a BGO imaging calorimeter, and a neutron detector (NUD). Compared with the AMS-02 experiment, DAMPE has a better energy resolution and could measure CR electrons and positrons at higher energies up to 10 TeV.

Interestingly, the DAMPE $e^{\pm}$ spectrum shows a break at $\sim$ 0.9 TeV and a tentative peak at $\sim$ 1.4 TeV. Many studies have been performed to explain these spectral features [18-45]. Most of these studies focus on how to explain the tentative peak at $\sim$ 1.4 TeV in specific DM models, while

*Corresponding author (email: yinpf@ihep.ac.cn)

refs. [18, 25] systematically study this feature in the general scenarios of DM and astrophysical sources. In order to explain the break structure at ~ 0.9 TeV, ref. [19] investigates the contribution of electrons that are released at the final stage of the evolution of supernova remnants (SNRs).

In this work, we explain the DAMPE $e^{\pm}$ result in the DM annihilation and pulsar scenarios, performing a fit to both the DAMPE $e^{\pm}$ spectrum and the AMS-02 positron fraction. The tentative feature at ~ 1.4 TeV is not considered in this analysis. Several leptonic DM annihilation channels to $\mu^+\mu^-$, $\tau^+\tau^-$, 4μ, 4τ, and mixed charged lepton final states $e^+e^- + \mu^+\mu^- + \tau^+\tau^-$ (denoted by $e\mu\tau$ for simplicity) are tested in the fit. Compared with the study of ref. [18], we adopt a different propagation parameter set, which can well explain the latest CR B/C and proton data. The comparison between the predicted $e^{\pm}$ spectra for different propagation parameter models is also shown.

In the pulsar scenario, we investigate 21 nearby pulsars in the ATNF catalog [46] [1] and find out some candidates that can be the single primary source of high energy $e^{\pm}$. Compared with the analysis of ref. [18] using a pseudo source, the framework considering the known pulsars in this work is more realistic. Furthermore, since the nearby pulsar may lead to a significant anisotropy in the $e^{\pm}$ flux, we also use the result of the Fermi-LAT anisotropy measurement to set constraint on the pulsar accounting for high energy $e^{\pm}$. Our results show that it is difficult to discriminate between the DM and pulsar explanations with the current DAMPE data.

This paper is organized as follows. In sect. 2, we introduce the CR propagation model adopted in this analysis. In sect. 3, we show the injection spectra of CR $e^{\pm}$ from the background, DM annihilation, and single nearby pulsar. In sect. 4, we explain the DAMPE $e^{\pm}$ spectrum in the DM annihilation and the single pulsar scenarios. Finally, the conclusion is given in sect. 5.

2 CR $e^{\pm}$ propagation in the Galaxy

Galactic SNRs are generally believed to be the main source of primary CR particles with energies below ~ 10^{17} eV. After leaving the source, CR particles travel along the trajectories which are tangled by the Galactic magnetic field, and thus diffusively propagate. Furthermore, they would also suffer from the so-called re-acceleration effect by scattering with the moving magnetic turbulence and gaining energy through the second order Fermi acceleration.

CRs propagate within a magnetic cylindrical diffusion halo with a characteristic radius of 20 kpc and a half height $z_h \sim O(1)$ kpc. At the boundary of the propagation halo, CRs would freely escape. During the journey to the earth, CRs lose their energies through a variety of effects; the primary nucleons fragment through inelastic collisions with the interstellar medium (ISM) and create secondary CR particles.

Involving the diffusion, re-acceleration, momentum loss and fragmentation effects, the transport equation can be described as [47, 48]:

$$\frac{\partial \Psi(\mathbf{r}, p, t)}{\partial t} = Q(\mathbf{r}, p) + \nabla \cdot (D_{xx} \nabla \Psi) + \frac{\partial}{\partial p} p^2 D_{pp} \frac{\partial}{\partial p} \frac{1}{p^2} \Psi - \frac{\partial}{p} \dot{p} \Psi - \frac{\Psi}{\tau_f}, \quad (1)$$

where $\Psi(\mathbf{r}, p, t)$ is the CR density per unit momentum interval at $\mathbf{r}$, $Q(\mathbf{r}, p)$ is the source term including primary and spallation contributions, D_{xx} is the spatial diffusion coefficient, D_{pp} is the diffusion coefficient in momentum space, τ_f is the time scale for the loss by fragmentation. We use the public code GALPROP [49] [2] to numerically solve this equation.

The spatial diffusion coefficient is described by

$$D_{xx} = \beta^{\eta} D_0 \left(\frac{R}{R_0} \right)^{\delta}, \quad (2)$$

where $\beta = v/c$ is velocity of particle in unit of the speed of light, D_0 is a normalization constant, $R = pc/ze$ is the rigidity, R_0 is the reference rigidity and η describes the velocity dependence of the diffusion coefficient.

The re-acceleration effect can be described by the diffusion in the momentum space. The momentum diffusion coefficient D_{pp} and spatial diffusion coefficient D_{xx} are related by [50]

$$D_{pp} = \frac{1}{D_{xx}} \cdot \frac{4 p^2 {V_A}^2}{3\delta(4-\delta)(4-\delta^2)\omega}, \quad (3)$$

where ω denotes the level of the interstellar turbulence, and V_A is Alfven velocity. We absorb ω to V_A and use V_A to characterize the re-acceleration strength.

In ref. [51] we have systematically studied the typical propagation models and nuclei injection spectra using the latest Boron-to-Carbon ratio data from AMS-02 and the proton fluxes from PAMELA and AMS-02. We find that the DR2 model including the re-acceleration and velocity dependent diffusion effects gives the best fit to all the data. The posterior mean values and 68% confidence interval of the model parameters are given in Table 1.

The local interstellar flux is given by $\Phi = \Psi(r_\odot)c/4\pi$. Before the local interstellar (LIS) CRs arrive at the earth, they suffer from the solar modulation effect within the heliosphere. We employ the force field approximation, which is described by a solar modulation potential ϕ, to deal with this effect.

1) http://www.atnf.csiro.au/people/pulsar/psrcat/
2) http:galprop.stanford.edu/

Table 1 The mean values and 1σ uncertainties of the propagation and proton injection parameters for the DR2 and DR propagation model

Parameters	DR2	DR
D_0 (10^{28} cm^2 s^{-1})	4.16 ± 0.57	7.24 ± 0.97
δ	0.500 ± 0.012	0.380 ± 0.007
z_h (kpc)	5.02 ± 0.86	5.93 ± 1.13
v_A (km s^{-1})	18.4 ± 2.0	38.5 ± 1.3
R_0 (GV)	4	4
η	-1.28 ± 0.22	1
$\log(A_p)$[3]	-8.334 ± 0.002	-8.347 ± 0.002
v_1	2.04 ± 0.03	1.69 ± 0.02
v_2	2.33 ± 0.01	2.37 ± 0.01
$\log(R^p_{br})$[4]	4.03 ± 0.03	4.11 ± 0.02

3 CR injection sources

The observed CR $e^{\pm}$ flux consists of three components: the primary electrons produced by SNRs; the secondary electrons and positrons from primary nuclei spallation processes in the ISM; $e^{\pm}$ pairs generated from exotic sources such as the DM or pulsar. The sum of the first two components is treated as the background. In this section, we outline the injection CR $e^{\pm}$ spectra for the backgrounds, DM annihilations, and single nearby pulsar.

3.1 The $e^{\pm}$ background spectrum

Ordinary CR sources are expected to be located around the Galactic disk, following the SNR radial distribution given by [52]

$$f(r,z) = (r/r_{\odot})^{1.25} \exp\left(-3.56 \cdot \frac{r-r_{\odot}}{r_{\odot}}\right) \exp\left(-\frac{|z|}{z_s}\right), \tag{4}$$

where $r_{\odot} = 8.3$ kpc is distance between the sun and the Galactic center, $z_s = 0.2$ kpc is the characteristic height of the Galactic disk.

These sources are able to accelerate the high energy CR electrons through the first order Fermi shock acceleration, which would result in a power law spectrum. The previous studies have found that a three-piece broken power law is enough to describe the injection spectrum of electrons below $\sim$ TeV [16, 53]. The break at a few GeV is used to fit the low energy data, while the hardening around hundreds of GeV is introduced to account for the effect of possible nearby sources [54] or non-linear particle acceleration [55].

Above TeV, the contribution to observed CR electrons would be dominated by several nearby SNRs due to the serious energy loss effect. The electron spectra from these SNRs may depend on their properties. The detailed discussions can be found in refs. [19, 56]. In this work, we simply introduce an exponential cutoff $\sim$ TeV to describe the behaviour of high energy injection spectra from the nearby SNRs. Thus, the injection spectrum of the primary electron component follows the form:

$$q(R) \propto \begin{cases} (R_{br}/R_{br0})^{\gamma_1} (R/R_{br0})^{-\gamma_0} \exp(E/E_{bgc}), & R <= R_{br0}, \\ (R/R_{br})^{-\gamma_1} \exp(E/E_{bgc}), & R <= R_{br}, \\ (R/R_{br})^{-\gamma_2} \exp(E/E_{bgc}), & R > R_{br}. \end{cases} \tag{5}$$

The source function $Q(\mathbf{r}, p)$ in eq. (1) for SNRs is given by $Q(\mathbf{r}, p) = f(r,z) \cdot q(R)$.

The secondary $e^{\pm}$s are produced by the spallation of primary CR particles (mainly protons and helium nuclei) in the ISM. The steady-state production rate of the secondary $e^{\pm}$ at the position $\mathbf{r}$ is

$$Q_{\rm sec}(\mathbf{r}, E) = 4\pi \sum_{ij} \int \mathrm{d}E' \Phi_i(E', \mathbf{r}) \frac{\mathrm{d}\sigma_{ij}(E', E)}{\mathrm{d}E} n_j(\mathbf{r}), \tag{6}$$

where $\mathrm{d}\sigma_{ij}(E', E)/\mathrm{d}E$ is the differential cross section for $e^{\pm}$ with the kinetic energy of E from the interaction between the CR particle i with the energy of E' and ISM target j, and n_j is the number density of the ISM target j.

3.2 $e^{\pm}$ from DM annihilations

The Galaxy is embedded in a huge DM halo. If DM particles have some interactions with standard model particles, the DM annihilation product could be an exotic source of CRs. The source term for DM annihilations is given by

$$Q_{\rm DM}(\mathbf{r}, E) = \frac{1}{2} \frac{\rho_{\rm DM}(\mathbf{r})^2}{m_{\rm DM}} \langle \sigma v \rangle \sum_k B_k \frac{\mathrm{d}N^k_{e^{\pm}}}{\mathrm{d}E}, \tag{7}$$

where $\mathrm{d}N^k_{e\pm}/\mathrm{d}E$ denotes the $e^{\pm}$ energy spectrum from a single annihilation with final states k, B_k is the corresponding branching fraction, ρ is the DM density, and $\langle \sigma v \rangle$ is thermal averaged velocity-weighted annihilation cross section. In our analysis, we adopt the Navarro-Frenk-White (NFW) density profile [57]:

$$\rho_{\rm DM}(\mathbf{r}) = \frac{\rho_s}{(|\mathbf{r}|/r_s)(1+|\mathbf{r}|/r_s)^2}, \tag{8}$$

where $r_s = 20$ kpc, and the local DM density is normalized to $\rho_{\odot} = 0.4$ GeV cm^{-3} to consist with the dynamical constraints [58-60]. The initial energy spectra of DM annihilation are taken from PPPC 4 DM ID [61] which includes the electroweak corrections. We also use GALPROP to simulate the propagation of such emissions from DM annihilation.

3) Propagated flux normalization at 100 GeV in unit of cm^{-2} s^{-1} sr^{-1} MeV^{-1}.
4) Break rigidity of proton injection spectrum in unit of MV.

3.3 $e^{\pm}$ from the nearby pulsar

The pulsar is a rotating neutron star surrounded by the strong magnetic field. It can produce $e^{\pm}$ pairs through the electromagnetic cascade and accelerate them by costing the spin-down energy. These high energy $e^{\pm}$ pairs are injected into the pulsar wind nebula (PWN) and finally escape to the ISM. A burst-like spectrum of the electron and positron is adopted to describe the pulsar injection, and is usually assumed to be a power law with an exponential cutoff:

$$Q_{\rm psr}(\mathbf{r}, E, t) = Q_0 E^{-\alpha} \exp\left(-\frac{E}{E_{\rm c}}\right)\delta(\mathbf{r})\delta(t), \tag{9}$$

where Q_0 is the normalization factor, α is the spectrum index, and $E_{\rm c}$ is the cutoff energy. The total energy output is related to the spin-down energy W_0 by assuming that a fraction f of W_0 would be transferred to $e^{\pm}$ pairs, so that

$$\int_{0.1\ \rm GeV}^{\infty} {\rm d}E E Q_0 E^{-\alpha} \exp\left(-\frac{E}{E_{\rm c}}\right) = \frac{f}{2} W_0. \tag{10}$$

W_0 can be derived from $\tau_0 \dot{E}(1 + t/\tau_0)^2$, where t is the pulsar age and the typical pulsar decay time is taken to be $\tau_0 = 10^4$ kyr here [12, 62].

Due to the high energy loss rate, the energetic $e^{\pm}$s could only propagate over a small distance of $O(1)$ kpc [63, 64]. For the local sources, we adopt an analytic solution of the propagation equation. The Green function solution without boundary condition is given by [65]

$$\Psi(r_{\odot}, E) = \frac{1}{(\pi\lambda^2(E, E_{\rm s}))^{3/2}} \cdot \frac{b(E_{\rm s})}{b(E)} \exp\left(-\frac{r^2}{\lambda^2(E, E_{\rm s})}\right) \times Q_{\rm psr}(E_{\rm s}), \tag{11}$$

where r is the distance to the pulsar, $E_{\rm s}$ is the initial $e^{\pm}$ energy from the source, $b(E) \equiv -{\rm d}E/{\rm d}t$ is the energy loss rate of $e^{\pm}$ and λ is the diffusion length defined as:

$$\lambda^2 \equiv 4 \int_{E}^{E_{\rm s}} {\rm d}E' D(E')/b(E'). \tag{12}$$

The $E_{\rm s}$ could be derived from the propagation time t and the final energy E by the relation of

$$\int_{E_{\rm s}}^{E} -\frac{{\rm d}E}{b(E)} = \int_{-t}^{0} {\rm d}t. \tag{13}$$

We include the energy loss induced by the synchrotron radiation in the Galactic magnetic field and the inverse Compton scattering with the ambient photon field. The local interstellar radiation field (ISRF) is taken from M1 model in ref. [66] and the magnetic field is assumed to be 4 μG. A detailed discussion on the relativistic energy loss rate is given in Appendix A1. As no simple analytic solution is available, we use GNU Scientific Library (GSL) [5] to numerically solve eq. (13).

4 Explanations of the DAMPE $e^{\pm}$ spectrum

The DAMPE collaboration has reported the $e^{\pm}$ spectrum with high resolution from 25 GeV to 4.6 TeV [17]. In this section, we fit the DAMPE data in the DM annihilation and single pulsar scenarios. The AMS-02 positron fraction [67] is also considered in the fit. Since we focus on the high energy $e^{\pm}$, the positron fraction data below 10 GeV are not adopted. There are 81 data points involved in the analysis.

4.1 The DM scenario

DM particles in the propagation halo may decay or annihilate to standard model particles and contribute to the finally observed CR leptons [68-70]. In this work, we discuss the DM annihilation channels to $\mu^+\mu^-$, $\tau^+\tau^-$, $e\mu\tau$, 4μ, and 4τ. In the $e\mu\tau$ channel, we set the branch ratios of e^+e^-, $\mu^+\mu^-$ and $\tau^+\tau^-$ final states to be free parameters. With the DR2 propagation parameters and proton injections given in Table 1, we vary the injection of primary electrons, DM parameters and solar modulation potential to obtain the best-fit though the Monte Carlo Markov Chain (MCMC) method. Note that we only consider the energy region above 10 GeV, thus the low energy break around several GeV in the background electron spectrum is neglected. In addition, a rescale factor $c_{e^{\pm}}$ is introduced to indicate the uncertainty of the hadronic collisions. The degree of freedom (d.o.f.) in this fitting is thus 72 except the $e\mu\tau$ model with d.o.f. 70 [6].

We list the best-fit results in Table 2 and show the spectra in Figure 1. With a large χ^2 valued 113.3, the $\mu^+\mu^-$ channel is excluded with more than 3σ confidence, while all the other channels provide reasonable fits. This is because that the $\mu^+\mu^-$ channel induces a harder $e^{\pm}$ spectrum than all the other channels, and tends to produce too many positrons at high energies when explaining the positron fraction below 100 GeV.

Note that the fit for annihilation channels with hard DM contributions is sensitive to the secondary positrons. Yuan et al. [18] performed a similar analysis but with a smaller diffusion coefficient power index $\delta = 1/3$. Since this δ leads to a harder secondary positron spectrum, the $\mu^+\mu^-$ channel works well in that analysis. In order to illustrate the impact of the propagation parameters on the fitting result, we perform a fit

5) https://www.gnu.org/software/gsl/

6) There is also a normalize factor of the injection spectrum A_e, which is not quite relevant but is still taken as a free parameter.

Table 2 Posterior mean and 68% credible uncertainties of the model parameters and χ^2 value in the DM scenarios, with d.o.f. of 72 except the $e\mu\tau$ model with d.o.f 70

Parameters	$\mu^+\mu^-$	$\tau^+\tau^-$	$e\mu\tau$	4μ	4τ
γ_1	3.05 ± 0.02	2.93 ± 0.02	2.93 ± 0.03	3.06 ± 0.01	2.90 ± 0.02
γ_2	2.57 ± 0.02	2.50 ± 0.02	2.53 ± 0.02	2.53 ± 0.02	2.50 ± 0.02
$\log(R^e_{br}(\mathrm{MV}))$	4.69 ± 0.03	4.70 ± 0.04	4.73 ± 0.03	4.71 ± 0.03	4.68 ± 0.04
$c_{e^\pm}$	3.66 ± 0.03	2.82 ± 0.09	3.07 ± 0.19	3.67 ± 0.04	2.65 ± 0.03
E_{bgc}(TeV)	4.42 ± 0.96	6.2 ± 2.0	10.9 ± 2.2	4.17 ± 1.09	5.58 ± 0.71
ϕ(GV)	1.48 ± 0.02	0.77 ± 0.10	1.16 ± 0.17	1.30 ± 0.08	0.67 ± 0.07
m_{DM} (GeV)	1891 ± 71	3210 ± 316	1560 ± 178	3243 ± 290	5366 ± 338
$\langle\sigma v\rangle(10^{-23}\mathrm{cm}^3\ \mathrm{s}^{-1})$	1.37 ± 0.09	5.24 ± 0.82	1.46 ± 0.31	2.25 ± 0.37	7.96 ± 1.01
χ^2	113.30	68.71	59.69	89.87	69.56

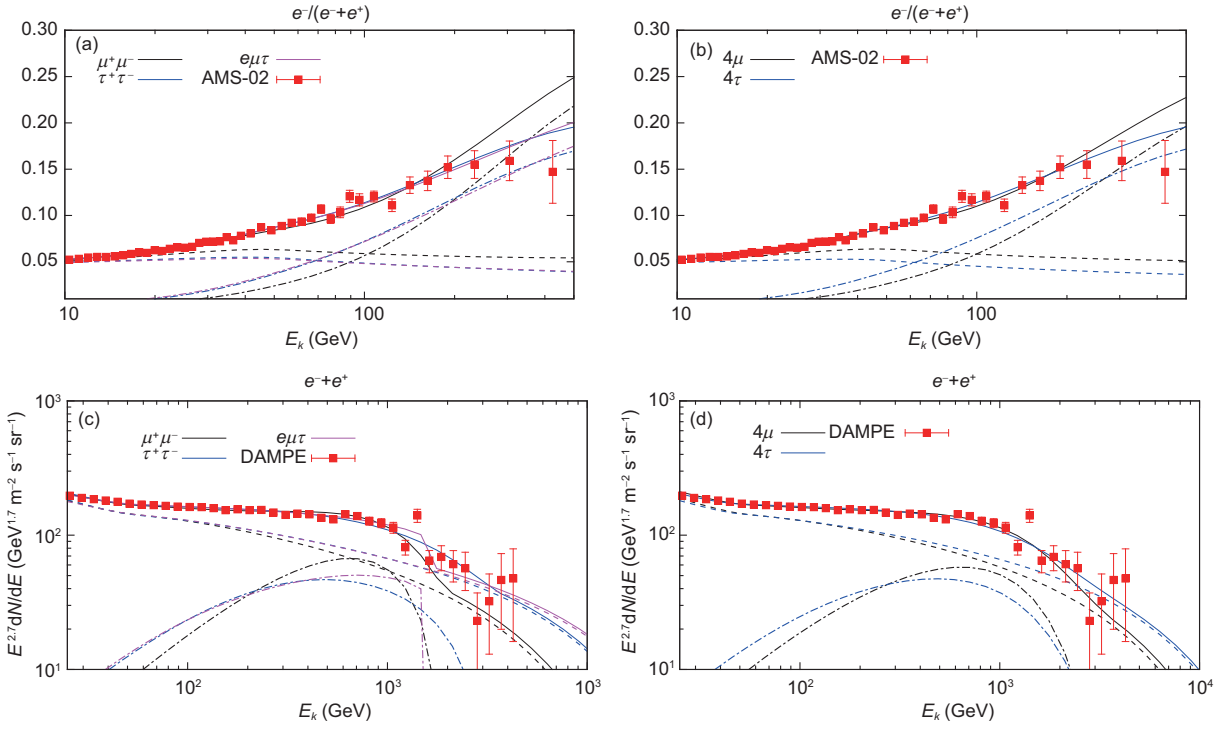

Figure 1 (Color online) The spectra of the best-fit results in the DM scenario. (a), (b) The positron fractions in comparison with the AMS-02 data [67]; (c), (d) the total $e^\pm$ spectra in comparison with the DAMPE data [17]. The dashed, dotted-dashed and solid lines represent the backgrounds, DM contributions and total results, respectively.

for the $\mu^+\mu^-$ channel using the DR best-fit parameters from ref. [51] with $\delta = 0.38$, and also find an acceptable χ^2 of ~ 79. We also list the DR parameters in Table 1. The corresponding best-fit spectra are shown in Figure 2 in comparison with the spectra derived from the DR2 model adopted in this work. Therefore, taking into account the current uncertainty of propagation effects, the $\mu^+\mu^-$ channel would be still acceptable.

In the fit for the $e\mu\tau$ channel, since the sharp shapes of the injection spectra from the $\mu^\pm$ and $e^\pm$ final states are not favoured here, the $\tau^\pm$ final states are dominant with a branch ratio of 0.755, while he branch ratios of $e^\pm$ and $\mu^\pm$ are 0.094 and 0.151 respectively. A recent work also analysed this channel but found that the branch ratio of $\tau^\pm$ is suppressed [26]. This different conclusion may be attributed to that their background secondary positron spectrum is much harder than ours. It is interesting to note that the contribution from the $e\mu\tau$ final states would indicate a distinct drop in the spectrum at the DM mass, as shown in Figure 1(c). It is possible to check such spectra feature with the results of DAMPE or HERD in the future.

In Figure 3, we show the distribution and 68%, 95% confidence regions for the DM mass and thermally averaged annihilation cross section. Note that the DM implication for the

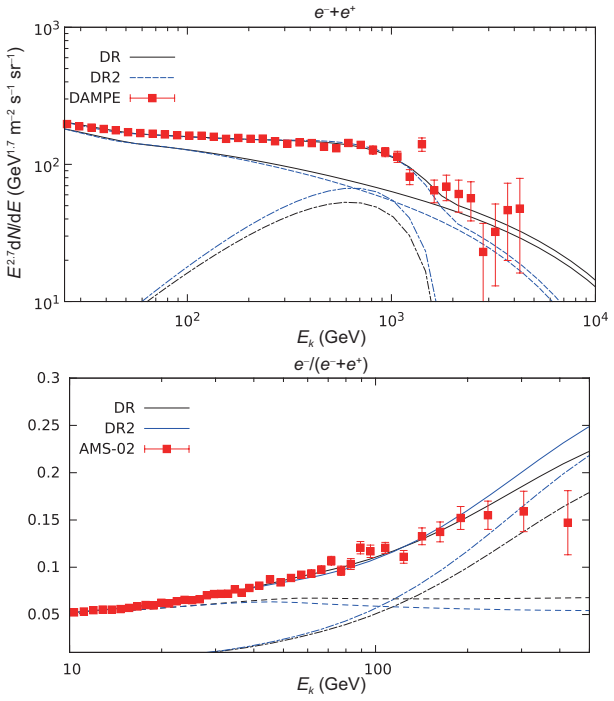

Figure 2 (Color online) Similar to Figure 1, but for the $\mu^+\mu^-$ channel using the DR and DR2 propagation model in ref. [51].

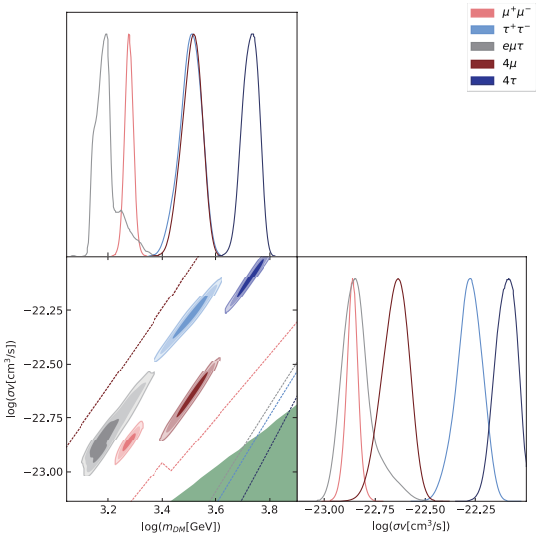

Figure 3 (Color online) The distributions and 68%, 95% confidence regions of the DM mass versus thermally averaged annihilation cross section. Different colors correspond to different channels. The top left and bottom right panels show the parameter distributions. At the bottom left panel, the 95% confidence limits for corresponding channels derived from the Fermi-LAT gamma-ray observations of dwarf galaxies [76] are also shown in dash line. The dark green shaded region represents the constraint from the Planck observations of CMB anisotropies, with an energy deposition efficiency $f_{\rm eff}$ ranged from 0.15 to 0.7 [72].

CR $e^{\pm}$ excess has been strongly constrained by many other observations, such as the cosmic microwave background (CMB) [71-73], dwarf galaxy gamma-ray [74], and diffuse gamma-ray observations [75]. We also show the corresponding constraints in Figure 3. To calculate the constraints from dwarf galaxies, we use PPPC 4 DM ID [61] to produce the DM gamma-ray spectra and adopt the likelihood results from the combined analysis given in ref. [76]. The constraints from the CMB observations are taken from ref. [18], where the Planck 2015 results with an energy deposition efficiency $f_{\rm eff}$ ranged from 0.15 to 0.7 [72] are adopted. The best-fit regions for many channels shown in Figure 3 seem to be excluded. However, the tensions between these observations can be reconciled in the velocity-dependent annihilation scenario due to the fact that DM particles contributing to these observations have different typical relative velocities [77, 78].

On the other hand, the constraints from the diffuse gamma-ray observation [75] cannot be easily avoided in the velocity-dependent annihilation scenario. However, the astrophysical uncertainties of this analysis arising from the Galactic CR model are not negligible. The solid constraints given by the Fermi-LAT collaboration without modeling of the astrophysical background cannot exclude the DM implication accounting for the CR $e^{\pm}$ excess. When the contributions of the pion decay and inverse Compton scattering from Galactic CRs are considered, the constraints given by the Fermi-LAT collaboration become stringent and strongly disfavor the $\tau^+\tau^-$ channel. However, these constraints depend on the CR distribution in the galaxy. In order to reduce the related uncertainties, more precise data and further studies on the CR model will be needed.

4.2 The single pulsar scenario

The nearby pulsars are possible sources of high energy CR $e^{\pm}$. The contribution from multiply local pulsars may results in fluctuations in the spectrum [13, 63]. For the simplicity, we consider the cases in which a nearby mature pulsar is the primary source of high energy $e^{\pm}$ here. The 21 known pulsars within 1 kpc with characteristic ages in the range of 10^3-10^6 years are considered. Their properties, such as the distance, age and spin-down luminosity, are taken from the ATNF catalog [46] [7)], which includes the most exhaustive and updated list of known pulsars.

In this section, we fit the DAMPE total $e^{\pm}$ spectrum and the AMS-02 positron fraction using one of the 21 selected pulsars. Comparing with the DM scenario with two free parameters, there are three free parameters (f, α, E_c) in the pulsar scenario. Thus the d.o.f. is 71 in the fit. Then, we drop all the candidates which are not acceptable at 95.4% C.L., and

7) http://www.atnf.csiro.au/people/pulsar/psrcat/

list the best-fit results of the five left pulsars in Table 3.

In the estimation of the injection energy, the transfer fraction f is supposed to vary from 1% to 30%, while τ_0 is taken to be 10^4 years as a typical value. However, since the value of τ_0 can vary between 10^3-10^4 years, the estimated spin-down energies in some cases could be 10 times larger than this work. Considering these extreme cases, the transfer fraction f as large as 3 can be accepted here. Therefore, except for J0954-5430 with a very large transfer fraction of 7.58, we accept the other four pulsars listed in Table 3. For these four acceptable pulsars, we show the best-fit spectra in Figure 4. We find that B1001-47, which is older than the others, would lead to a drop around 1.2 TeV at the $e^{\pm}$ spectrum, due to the energy loss effect. This drop structure is similar to that of the spectrum derived from the $e\mu\tau$ channel in the DM scenario. Therefore, these two explanations would be difficult to be distinguished from only the $e^{\pm}$ spectrum measurement. From Figures 1 and 4, it can be seen that the best-fit spectra resulted from some pulsars are very similar to those induced by DM annihilation. It is still difficult to distinguish between these two explanations of high energy $e^{\pm}$ with the current DAMPE result.

In order to take account of the uncertainty from the injection spectrum of the pulsar, the 68% and 95% confidence regions for the power index α and cutoff energy E_c are shown in Figure 5. The favoured values of injection parameters depend on the age and distance of the pulsar. For the far or young pulsars, such as J1732-3131 and J0940-5428, the injected low energy positrons are difficult to reach the Earth, therefore a large α is necessary for enough positrons at low energies. In addition, the contributions from the old or far pulsars would suffer a serious energy loss effect, thus they require a high energy cutoff E_c to ensure enough high energy positrons.

The local young astrophysical sources may induce the observable dipole anisotropy in the CR arrival direction [79-82]. Therefore, the four pulsars considered above would be constrained by the current anisotropy observations. Both Fermi and AMS-02 have not detected a significant anisotropy, and

Table 3 Posterior mean, 68% credible uncertainties of the model parameters and χ^2 value in the single pulsar scenarios, with d.o.f. of 71

Parameters	J1732-3131	J0940-5428	B0656+14 (Monogem)	B1001-47	J0954-5430
γ_1	2.94 ± 0.03	2.93 ± 0.04	2.84 ± 0.03	2.80 ± 0.03	2.84 ± 0.03
γ_2	2.52 ± 0.02	2.51 ± 0.03	2.52 ± 0.03	2.50 ± 0.02	2.52 ± 0.02
$\log(R^e_{br}[\mathrm{MV}])$	4.72 ± 0.05	4.73 ± 0.05	4.81 ± 0.05	4.84 ± 0.04	4.81 ± 0.05
E_{bgc} (TeV)	6.41 ± 2.25	4.99 ± 2.67	5.93 ± 3.02	7.91 ± 1.56	6.82 ± 1.99
$c_{e^{\pm}}$	3.21 ± 0.22	3.18 ± 0.24	2.66 ± 0.13	2.37 ± 0.20	2.66 ± 0.13
ϕ (GV)	1.18 ± 0.22	1.17 ± 0.25	1.32 ± 0.14	1.18 ± 0.21	1.24 ± 0.18
f	3.59 ± 0.88	0.26 ± 0.07	2.86 ± 0.25	3.33 ± 0.26	7.58 ± 0.62
α	2.14 ± 0.06	2.08 ± 0.07	1.78 ± 0.05	1.82 ± 0.04	1.85 ± 0.04
E_c (TeV)	4.94 ± 2.12	2.12 ± 0.80	2.65 ± 0.93	6.50 ± 2.35	5.46 ± 1.89
d (kpc)	0.64	0.38	0.29	0.37	0.43
Age (kyr)	111	42.2	111	220	171
χ^2	59.82	62.98	56.13	60.64	56.39

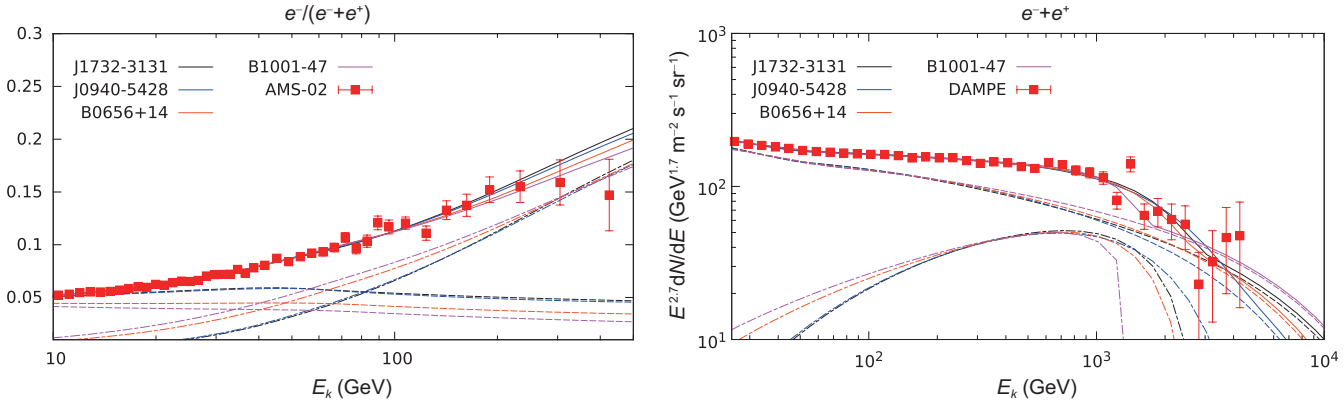

Figure 4 (Color online) The same as Figure 1, but for the single pulsar scenario.

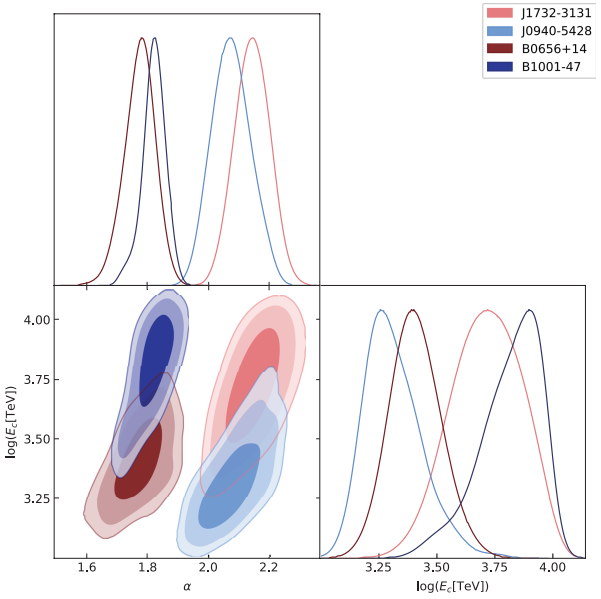

Figure 5 (Color online) Similar to Figure 3, but for the α and E_c in single pulsar scenario.

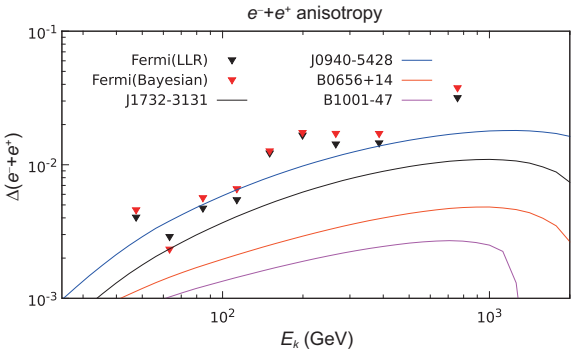

Figure 6 (Color online) The $e^{\pm}$ anisotropies for the pulsars. The 95% C.L. upper limits given by Fermi-LAT using the log-likelihood ratio and Bayesian methods [84] are also shown for comparison.

set upper limits on the CR electron-positron, positron and electron dipole anisotropies [83-86]. For the AMS-02 experiment [86], the 95% C.L. limit on the integrated positron dipole anisotropy above 16 GeV based on the first five years data is about 0.02. Recently, the Fermi collaboration has released the latest result of the dipole $e^{\pm}$ anisotropy, using seven years data reconstructed by Pass 8 in the energy region from 42 GeV to 2 TeV [84]. The 95% C.L. upper limit ranges from 3×10^{-3} to 3×10^{-2}.

For the single nearby source dominating the CR flux, the dipole anisotropy is given by [79]

$$\Delta = \frac{3D}{c}\left|\frac{\nabla\Phi}{\Phi}\right|. \tag{14}$$

By using the flux in eq. (11), we explicitly express the dipole anisotropy as:

$$\Delta(E) = \frac{3D(E)}{c}\frac{2r}{\lambda^2(E,E_s)}. \tag{15}$$

We estimate the positron anisotropy for the four pulsars, and find all of them would result in an integrated anisotropy obviously smaller than 0.02 at 16 GeV, which evade the limit of AMS-02. In addition, we show the expected $e^{\pm}$ anisotropy from each pulsar comparing with the measurement of Fermi-LAT in Figure 6. Note that the dipole anisotropy is proportional to the distance-to-age ratio r/t of the pulsar. We find that the anisotropy induced by J0940-5428 with a $r/t \sim 9\times10^{-3}$ kpc/kyr has a tension with the Fermi upper limit. For J1732-3131 with a larger age of 111 kyr and a smaller $r/t \sim 5.8\times10^{-3}$ kpc/kyr, there is a slight tension as the Fermi-LAT Bayesian limit excludes this source while the LLR limit does not. The other pulsars with a very small $r/t \sim 2.5\times10^{-3}$ kpc/kyr provides a very small anisotropy, which is far from the Fermi-LAT sensitivity. As a conclusion, B0656+14 and B1001-47 survive from all the limits considered.

Finally, we give some brief comments on the recent HWAC results of two pulsars Geminga and PSR B0656+14 [87]. The extended gamma-ray emissions from these pulsars detected by HAWC show that the diffusion coefficient around the $e^{\pm}$ source is much smaller than the convention expectation. This indicates that $e^{\pm}$s from the pulsar could not propagate to a large distance and may be insufficient to contribute to the observed positron in the Solar system. However, the region leading to this inefficient diffusion should not be large, in order to keep consistent with the measurement of secondary-to-primary CR ratios [88]. If the typical size of the inefficient diffusion region around the pulsar is only several tens of pc, the pulsar contribution to the observed $e^{\pm}$ flux would be still sufficient [89, 90].

5 Conclusion

In this paper, we study the DM annihilation and pulsar interpretations of high energy CR $e^{\pm}$ observed by DAMPE. We investigate the $e^{\pm}$ contributions from several DM annihilation channels and known nearby pulsars in the ATNF catalog, and find some allowed realizations.

For the DM scenario, we investigate the $\mu^+\mu^-$, $\tau^+\tau^-$, $e\mu\tau$, 4μ, and 4τ annihilation channels. The constraints from the diffuse γ ray, the γ ray of dwarf galaxy and the CMB observations are discussed. We find that all these channels except the $\mu^+\mu^-$ channel can explain the DAMPE data well. The explanation of the $\mu^+\mu^-$ channel would be sensitive to the propagation model. In the $e\mu\tau$ mixing channel, the $\tau^{\pm}$ final states are dominant. However, the contribution from the $e^{\pm}$ final states in this channel would lead to a distinct drop in the spectrum. Such spectral feature may be detected in the

future measurements with larger statistics, such as DAMPE and HERD. We find that many channels have been excluded and some complicated DM models are necessary to reconcile the tension between different observations.

For the pulsar scenario, we find five single pulsars that are acceptable at 94.5% C.L. Among these pulsars, J0954-5430 requires a too large transfer efficiency which is unacceptable. We also investigate the $e^{\pm}$ anisotropy from the single pulsar, and find that J1732-3131 and J0940-5428 are not favored by the Fermi-LAT observations. As a conclusion, B0656+14 and B1001-47 are possible to explain the current observations of DAMPE and AMS-02. In addition, the old pulsar B1001-47 would also lead to a drop in the $e^{\pm}$ spectrum due to the energy loss effect. This drop is difficult to be distinguished from that of the $e\mu\tau$ channel. Our results show that it is difficult to distinguish between the DM annihilation and single pulsar explanations of high energy $e^{\pm}$ with the current DAMPE result. In the future, the combination of the $e^{\pm}$ spectra and anisotropy measurements with large statistics like HERD may be useful in further discriminating the origins of high energy CR $e^{\pm}$.

This work was supported by the National Key Program for Research and Development (Grant No. 2016YFA0400200), and the National Natural Science Foundation of China (Grant Nos. U1738209, 11475189, and 11475191).

1 O. Adriani, et al. (PAMELA Collaboration), Nature **458**, 607 (2009), arXiv: 0810.4995.
2 M. Aguilar, et al. (AMS Collaboration), Phys. Rev. Lett. **113**, 121102 (2014).
3 L. Bergström, T. Bringmann, and J. Edsjö, Phys. Rev. D **78**, 103520 (2008), arXiv: 0808.3725.
4 V. Barger, W. Y. Keung, D. Marfatia, and G. Shaughnessy, Phys. Lett. B **672**, 141 (2009), arXiv: 0809.0162.
5 M. Cirelli, M. Kadastik, M. Raidal, and A. Strumia, Nucl. Phys. B **813**, 1 (2009), arXiv: 0809.2409; M. Cirelli, M. Kadastik, M. Raidal, and A. Strumia, Nucl. Phys. B **873**, 530 (2013).
6 P. Yin, Q. Yuan, J. Liu, J. Zhang, X. Bi, S. Zhu, and X. Zhang, Phys. Rev. D **79**, 023512 (2009), arXiv: 0811.0176.
7 J. Zhang, X. J. Bi, J. Liu, S. M. Liu, P. F. Yin, Q. Yuan, and S. H. Zhu, Phys. Rev. D **80**, 023007 (2009), arXiv: 0812.0522.
8 N. Arkani-Hamed, D. P. Finkbeiner, T. R. Slatyer, and N. Weiner, Phys. Rev. D **79**, 015014 (2009), arXiv: 0810.0713.
9 M. Pospelov, and A. Ritz, Phys. Lett. B **671**, 391 (2009), arXiv: 0810.1502.
10 H. Yüksel, M. D. Kistler, and T. Stanev, Phys. Rev. Lett. **103**, 051101 (2009), arXiv: 0810.2784.
11 D. Hooper, P. Blasi, and P. D. Serpico, J. Cosmol. Astropart. Phys. **2009**, 025 (2009), arXiv: 0810.1527.
12 S. Profumo, Open Phys. **10**, 1 (2012), arXiv: 0812.4457.
13 D. Malyshev, I. Cholis, and J. Gelfand, Phys. Rev. D **80**, 063005 (2009), arXiv: 0903.1310.
14 P. Blasi, Phys. Rev. Lett. **103**, 051104 (2009), arXiv: 0903.2794.
15 H. B. Hu, Q. Yuan, B. Wang, C. Fan, J. L. Zhang, and X. J. Bi, Astrophys. J. **700**, L170 (2009), arXiv: 0901.1520.
16 S. J. Lin, Q. Yuan, and X. J. Bi, Phys. Rev. D **91**, 063508 (2015), arXiv: 1409.6248.
17 G. Ambrosi, et al. (DAMPE Collaboration), Nature **552**, 63 (2017), arXiv: 1711.10981.
18 Q. Yuan, L. Feng, P.-F. Yin Y.-Z. Fan, X.-J. Bi, M.-Y. Cui, T.-K. Dong, Y.-Q. Guo, K. Fang, H.-B. Hu, X. Y. Huang, S.-J. Lei, X. Li, S.-J. Lin, H. Liu, P.-X. Ma, W.-X. Peng, R. Qiao, Z.-Q. Shen, M. Su, Y.-F. Wei, Z.-L. Xu, C.n Yue, J.-J. Zang, C. Zhang, X. M. Zhang, Y.-P. Zhang, Y.-J. Zhang, and Y.-L. Zhang, arXiv: 1711.10989.
19 K. Fang, X. J. Bi, and P. F. Yin, Astrophys. J. **854**, 57 (2018), arXiv: 1711.10996.
20 Y.-Z. Fan, W.-C. Huang, M. Spinrath, Y.-L. S. Tsai, and Q. Yuan, arXiv: 1711.10995.
21 G. H. Duan, L. Feng, F. Wang, L. Wu, J. M. Yang, and R. Zheng, J. High Energ. Phys. **2018**, 107 (2018), arXiv: 1711.11012.
22 P. Athron, C. Balazs, A. Fowlie, and Y. Zhang, J. High Energ. Phys. **2018**, 121 (2018), arXiv: 1711.11376.
23 J.-J Cao, L. Feng, X.-F. Guo, L.-L. Shang, F. Wang, and P.-W. Wu, arXiv: 1711.11452.
24 X.-W. Liu, and Z.-W. Liu, arXiv: 1711.11579.
25 X.-J. Huang, Y.-L. Wu, W.-H. Zhang, and Y.-F. Zhou, arXiv: 1712.00005.
26 J.-S. Niu, T.-J. Li, R. Ding, B. Zhu, H.-F. Xue, and Y. Wang, arXiv: 1712.00372.
27 Y. Gao, and Y.-Z. Ma, arXiv: 1712.00370.
28 F.-W. Yang, M. Su, and Y. Zhao, arXiv: 1712.01724.
29 J.-J. Cao, L Feng, X.-F. Guo, L.-L. Shang, F. Wang, P.-W. Wu, and L. Zu, Eur. Phys. J. C **78**, 198 (2018).
30 K. Ghorbani, and P. H. Ghorbani, arXiv: 1712.01239.
31 T. Nomura, and H. Okada, arXiv: 1712.00941.
32 P.-H. Gu, arXiv: 1712.00922.
33 R.-L. Zhu, and Y. Zhang, arXiv: 1712.01143.
34 T. Li, N. Okada, and Q. Shafi, Phys. Lett. B **779**, 130 (2018), arXiv: 1712.00869.
35 C.-H. Chen, C.-W. Chiang, and T. Nomura, arXiv: 1712.00793.
36 H.-B. Jin, B. Yue, X. Zhang, and X. Chen, arXiv: 1712.00362.
37 G. H. Duan, X.-G. He, L. Wu, and J. M. Yang, arXiv: 1711.11563.
38 L. Zu, C. Zhang, L. Feng, Q. Yuan, and Y.-Z. Fan, arXiv: 1711.11052.
39 R. Ding, Z.-L. Han, L. Feng, and B. Zhu, arXiv: 1712.02021.
40 P.-H. Gu, arXiv: 1711.11333.
41 W. Chao, and Q. Yuan, arXiv: 1711.11182.
42 Y.-L. Tang, L. Wu, M. Zhang, and R. Zheng, arXiv: 1711.11058.
43 P. H. Gu, and X. G. He, Phys. Lett. B **778**, 292 (2018), arXiv: 1711.11000.
44 G. Liu, F. Wang, W. Wang, and J. M. Yang, Chin. Phys. C **42**, 035101 (2018), arXiv: 1712.02381.
45 S.-F. Ge, and H.-J. He, arXiv: 1712.02744.
46 R. N. Manchester, G. B. Hobbs, A. Teoh, and M. Hobbs, Astron. J. **129**, 1993 (2005).
47 V. L. Ginzburg, and S. I. Syrovatsky, Prog. Theor. Phys. Suppl. **20**, 1 (1961).
48 V. L. Ginzburg, and V. S. Berezinskiĭ, *Astrophysics of Cosmic Rays* (Elsevier, Amsterdam, 1990).
49 A. W. Strong, I. V. Moskalenko, T. A. Porter, G. Jóhannesson, E. Orlando, and S. W. Digel, arXiv: 0907.0559.
50 E. S. Seo, and V. S. Ptuskin, Astrophys. J. **431**, 705 (1994).
51 Q. Yuan, S. J. Lin, K. Fang, and X. J. Bi, Phys. Rev. D **95**, 083007 (2017), arXiv: 1701.06149.
52 R. Trotta, G. Jóhannesson, I. V. Moskalenko, T. A. Porter, R. Ruiz de Austri, and A. W. Strong, Astrophys. J. **729**, 106 (2011), arXiv: 1011.0037.
53 I. V. Moskalenko, and A. W. Strong, Astrophys. J. **493**, 694 (1998).
54 G. Bernard, T. Delahaye, Y. Y. Keum, W. Liu, P. Salati, and R. Taillet, Astron. Astrophys. **555**, A48 (2013), arXiv: 1207.4670.
55 V. Ptuskin, V. Zirakashvili, and E. S. Seo, Astrophys. J. **763**, 47 (2013), arXiv: 1212.0381.
56 K. Fang, B. B. Wang, X. J. Bi, S. J. Lin, and P. F. Yin, Astrophys. J.

836, 172 (2017), arXiv: 1611.10292.
57 J. F. Navarro, C. S. Frenk, and S. D. M. White, Astrophys. J. **490**, 493 (1997).
58 F. Nesti, and P. Salucci, J. Cosmol. Astropart. Phys. **2013**, 016 (2013), arXiv: 1304.5127.
59 Y. Sofue, Publ Astron Soc Jpn **64**, 75 (2012), arXiv: 1110.4431.
60 M. Weber, and W. de Boer, Astron. Astrophys. **509**, A25 (2010), arXiv: 0910.4272.
61 M. Cirelli, G. Corcella, A. Hektor, G. Hütsi, M. Kadastik, P. Panci, M. Raidal, F. Sala, and A. Strumia, J. Cosmol. Astropart. Phys. **2011**, 051 (2011), arXiv: 1012.4515; J. Cosmol. Astropart. Phys. **2012**, E01 (2012).
62 F. A. Aharonian, A. M. Atoyan, and H. J. Volk, Astron. Astrophys. **294**, L41 (1995).
63 P. F. Yin, Z. H. Yu, Q. Yuan, and X. J. Bi, Phys. Rev. D **88**, 023001 (2013), arXiv: 1304.4128.
64 J. Feng, and H. H. Zhang, Eur. Phys. J. C **76**, 229 (2016), arXiv: 1504.03312.
65 A. M. Atoyan, F. A. Aharonian, and H. J. Völk, Phys. Rev. D **52**, 3265 (1995).
66 T. Delahaye, J. Lavalle, R. Lineros, F. Donato, and N. Fornengo, Astron. Astrophys. **524**, A51 (2010), arXiv: 1002.1910.
67 L. Accardo, et al. (AMS Collaboration), Phys. Rev. Lett. **113**, 121101 (2014).
68 L. Bergström, Rep. Prog. Phys. **63**, 793 (2000).
69 G. Bertone, D. Hooper, and J. Silk, Phys. Rep. **405**, 279 (2005).
70 L. Bergström, New J. Phys. **11**, 105006 (2009), arXiv: 0903.4849.
71 E. Komatsu, J. Dunkley, M. R. Nolta, C. L. Bennett, B. Gold, G. Hinshaw, N. Jarosik, D. Larson, M. Limon, L. Page, D. N. Spergel, M. Halpern, R. S. Hill, A. Kogut, S. S. Meyer, G. S. Tucker, J. L. Weiland, E. Wollack, and E. L. Wright, Astrophys. J. Suppl. Ser. **180**, 330 (2009), arXiv: 0803.0547.
72 P. A. R. Ade, et al. (Planck Collaboration), Astron. Astrophys. **594**, A13 (2016), arXiv: 1502.01589.
73 T. R. Slatyer, Phys. Rev. D **93**, 023527 (2016), arXiv: 1506.03811.
74 M. Ackermann, et al. (The Fermi-LAT Collaboration), Phys. Rev. Lett. **115**, 231301 (2015), arXiv: 1503.02641.
75 M. Ackermann, et al. (The Fermi-LAT Collaboration), Astrophys. J. **761**, 91 (2012), arXiv: 1205.6474.
76 A. Albert, et al. (The Fermi-LAT and DES Collaborations), Astrophys. J. **834**, 110 (2017), arXiv: 1611.03184.
77 Y. Bai, J. Berger, and S. Lu, arXiv: 1706.09974.
78 Q. F. Xiang, X. J. Bi, S. J. Lin, and P. F. Yin, Phys. Lett. B **773**, 448 (2017), arXiv: 1707.09313.
79 C.-S. Shen, and C.-Y. Mao, Astrophys. Lett. **9**, 169 (1971).
80 T. Kobayashi, Y. Komori, K. Yoshida, and J. Nishimura, Astrophys. J. **601**, 340 (2004).
81 G. Di Bernardo, C. Evoli, D. Gaggero, D. Grasso, L. Maccione, and M. N. Mazziotta, Astropart. Phys. **34**, 528 (2011), arXiv: 1010.0174.
82 S. Manconi, M. D. Mauro, and F. Donato, J. Cosmol. Astropart. Phys. **2017**, 006 (2017), arXiv: 1611.06237.
83 M. Ackermann et al. (Fermi LAT Collaboration), Phys. Rev. D **82**, 092004 (2010), arXiv: 1008.3999.
84 S. Abdollahi, et al. (Fermi-LAT Collaboration), Phys. Rev. Lett. **118**, 091103 (2017), arXiv: 1703.01073.
85 M. Aguilar, et al. (AMS Collaboration), Phys. Rev. Lett. **110**, 141102 (2013).
86 G. La Vacca, and AMS-02 Collaboration, arXiv: 1612.08957.
87 A. U. Abeysekara, et al. (HAWC Collaboration), Science **358**, 911 (2017), arXiv: 1711.06223.
88 D. Hooper, I. Cholis, T. Linden, and K. Fang, Phys. Rev. D **96**, 103013 (2017), arXiv: 1702.08436.
89 K. Fang, X. J. Bi, P. F. Yin, and Q. Yuan, arXiv: 1803.02640.
90 S. Profumo, J. Reynoso-Cordova, N. Kaaz, and M. Silverman, Phys. Rev. D **97**, 123008 (2018), arXiv: 1803.09731.
91 R. Schlickeiser, *Cosmic Ray Astrophysics* (Springer Science & Business Media, Berlin, 2002).
92 R. Schlickeiser, and J. Ruppel, New J. Phys. **12**, 033044 (2010), arXiv: 0908.2183.
93 D. Khangulyan, F. A. Aharonian, and S. R. Kelner, Astrophys. J. **783**, 100 (2014), arXiv: 1310.7971.

Appendix A1 Energy loss and cutoff

By using eq. (13) we can derive the $e^{\pm}$ energy $E_{\rm s}$ in the source. The energy loss of $e^{\pm}$ above few GeV is mainly caused by the synchrotron radiation and inverse Compton scattering processes. The synchrotron radiation energy loss is given by

$$-\left(\frac{{\rm d}E}{{\rm d}t}\right)_{\rm syn} = \frac{4}{3}\sigma_{\rm T}cU_B{\gamma_e}^2, \tag{a1}$$

where $\sigma_{\rm T}$ is the Thomson scattering cross section ($\sigma_{\rm T} = 6.65\times10^{-25}{\rm cm}^2$), c is the speed of light, U_B is the magnetic field energy density, and $\gamma_e = E/m_ec^2$ is the Lorentz factor.

The energy loss caused by the inverse Compton scattering of $e^{\pm}$ with energies $E << (m_ec^2)^2/k_bT$ in the Thomson regime can be expressed by eq. (a1) with replacing U_B to the radiation field energy density ($U_{\rm rad}$). The energy density distribution of ISRF is described in sect. 3.3. In the Thomson approximation the energy loss rate can be given by $-\frac{{\rm d}E}{{\rm d}t} = b_0E^2$, where $b_0 = \frac{4}{3m_ec^2}\sigma_Tc(U_B + U_{\rm rad})$ is a constant. This number is often taken to be $O(10^{-16})\,{\rm GeV}^{-1}{\rm s}^{-1}$ [14,64]. Then we can derive the maximum energy of $e^{\pm}$ arriving at the solar system as:

$$\int_{E_{\rm s}}^{E}\frac{{\rm d}E}{-b_0E^2} = \int_{-t}^{0}{\rm d}t \quad\rightarrow\quad E = \frac{1}{b_0t + 1/E_{\rm s}} < \frac{1}{b_0t}. \tag{a2}$$

This indicates that the maximum energies of observed $e^{\pm}$ are

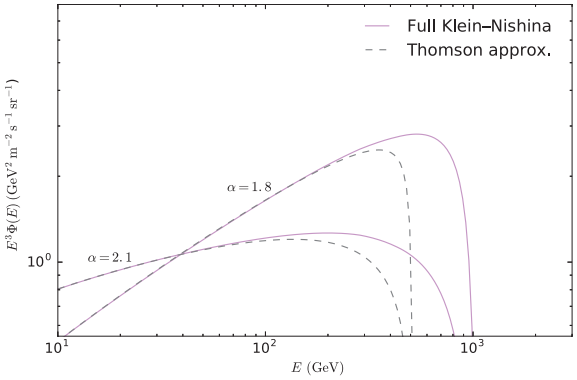

Figure a1 (Color online) Comparison between different treatments for the inverse Compton energy loss of the Geminga electron spectrum. The solid and dashed lines represented results for the relativistic energy loss rate and the Thomson approximation energy, respectively. α is the index of the injection spectrum.

determined by $1/b_0 t$ due to the energy loss and are almost independent of their initial energies from the source.

However, under the extreme Klein-Nishina limit with $E >> (m_e c^2)^2/k_b T$, the energy loss rate is

$$-\left(\frac{dE}{dt}\right)_{KN} = \frac{\sigma_T}{16}\frac{(m_e c k_b T)^2}{\hbar^3}\ln\frac{4\gamma_e k_b T}{m_e c^2} - 1.9805. \quad \text{(a3)}$$

In this case the energy loss rate only increases logarithmically with E, while it increases with E^2 under the Thomson limit. Thus the efficiency of inverse Compton scattering would be strongly reduced; this effect is referred to as "KLein-Nishina cutoff" [91] and has been discussed in refs. [66, 80, 92, 93]. In this work we adopt the parametrization expression in refs. [66] to accurately calculate the energy loss rate caused by the inverse Compton scattering.

For instance, we illustrate the Klein-Nishina effect for Geminga, which is a pulsar with a distance of 0.25 kpc, an age of 342 kyr, and a spin-down luminosity of 3.2×10^{34} erg/s. The energy transfer efficiency f is taken as 30% and the injection spectrum energy cutoff is assumed to be 10 TeV. As can be seen in Figure a1, since Thomson approximation results in a higher energy loss rate, the spectrum cutoff is sharper than that derived from the Klein-Nishina effect especially for a hard injection spectrum.